

Rotation periods and colours of 10-m scale near-Earth asteroids from CFHT target of opportunity streak photometry

B. T. Bolin,¹* † M. Ghosal,² and R. Jedicke²

¹*Goddard Space Flight Center, 8800 Greenbelt Road, Greenbelt, MD 20771, USA,*

²*Institute for Astronomy, University of Hawai'i, 2680 Woodlawn Dr., Honolulu, HI 96822, USA*

Accepted XXX. Received YYY; in original form ZZZ

ABSTRACT

The rotational properties of ~ 10 m-scale asteroids are poorly understood with only a few measurements. Additionally, collisions or thermal recoil can spin their rotations to periods less than a few seconds obfuscating their study due to the observational cadence imposed by the long read-out times of charge-coupled device imagers. We present a method to measure the rotation periods of 10 m-scale asteroids using the target of opportunity capability of the Canada France Hawaii Telescope and its MegaCam imager by intentionally streaking their detections in single exposures when they are at their brightest. Periodic changes in brightness as small as ~ 0.05 mag along the streak can be measured as short as a few seconds. Additionally, the streak photometry is taken in multiple g, r, and i filter exposures enabling the measurement of asteroid colours. The streak photometry method was tested on CFHT observations of three 10 m-scale asteroids, 2016 GE₁, 2016 CG₁₈, and 2016 EV₈₄. Our 3 targets are among the smallest known asteroids with measured rotation periods/colours having some of the shortest known rotation periods. We compare our rotation period and taxonomic results with independent data from the literature and discuss applications of the method to future small asteroid observations.

Key words: minor planets, asteroids: general

1 INTRODUCTION

Near Earth Asteroids (NEAs) represent a dynamically young sub-population of ejected Main Belt Asteroids (MBAs). They have short lifetimes on the order of millions of years ending in collisions with the inner planets, the Sun, or ejection from the solar system. While the understanding of the rotational properties of km or 100-m scale asteroids has improved (e.g., Thirouin et al. 2016; Szabó et al. 2016), the rotational properties of ~ 10 m scale asteroids are poorly understood with only a handful of measurements due, in part, to them being orders of magnitude fainter than larger asteroids. Additionally, the Yarkovsky-O'Keefe-Radzievskii-Paddack (YORP) effect, caused by the change in an asteroid's rotation due to the momentum imparted by re-emitted thermal radiation from solar heating, can spin up 10 m-scale NEAs within their dynamical lifetimes so that they have rotation periods of only a few seconds or less (Bottke et al. 2006; Vokrouhlický et al. 2015).

Studies on the structure of small asteroids have been mostly limited to computer modeling (e.g., Sánchez & Scheeres 2014). Some models suggest that small objects should be 'strong', perhaps monolithic objects (e.g., Bottke et al. 2005b,a) yet observations of some of the smallest asteroids suggest that they have low-densities (e.g., Micheli et al. 2014, 2013). The discovery of NEO 2008 TC₃ before its impact with Earth gave the first opportunity to study the structure of a meter-scale asteroid with observational data and meteoritic samples

(Jenniskens et al. 2010). The data indicated that 2008 TC₃ was a rapid tumbler less than a few meters in diameter and consisted of a heterogeneous mixture of materials implying it was a rubble pile (Kozubal et al. 2011). Other work has shown that small asteroids on the tens of meters scale tend to rotate above the limit allowed by the cohesive strength of rubble piles (Harris et al. 2009; Warner et al. 2009).

Information about the structural cohesion of asteroids 10 m or smaller in diameter is less known compared to larger asteroids. There are only 10 asteroids that are 10 m or smaller in diameter with known periods (e.g., Thirouin et al. 2016) and none are rotating faster than the theoretical bursting rate for rubble piles or solid rock (Sánchez & Scheeres 2014; Bolin et al. 2014). The lack of detection of rapidly-spinning asteroids may be the result of an observational bias. The YORP effect (Bottke et al. 2006; Vokrouhlický et al. 2015) can increase the rotation rate of 10 m NEAs to their theoretical bursting limits of < 10 radians/s in several orders of magnitude less time than their dynamical lifetimes of millions of years (Hirabayashi 2015; Nesvorný et al. 2023).

Additionally, the measurement of the short rotation periods of 10 m-scale asteroids is difficult due to their faintness. Main belt asteroids (MBAs) between 1 m and 10 m in size are too faint to be observed from Earth. Near-Earth asteroids (NEAs) in this size range can reach $V \sim 20$ or brighter when passing within a few lunar distances of the Earth (Jedicke et al. 2016). However, close-approaching NEAs are difficult to observe due to their high, ~ 10 s of $''$ per second, rates of motion when this close to the Earth, and are only observable for a few days at a time before they become too faint to observe by most fa-

* NASA Postdoctoral Program Fellow

† E-mail: bryce.bolin@nasa.gov (BTB)

cilities or go into solar conjunction (Bolin et al. 2020). Furthermore, the long observational cadence imposed by the typical ~10s of seconds read-out times of charge-coupled device (CCD) imagers makes detection of short rotation periods difficult (Jedicke et al. 2015). The majority of asteroid lightcurve observations use individual charge-coupled device (CCD) camera exposures, focusing on more distant and slower rotating asteroids such as MBAs (McNeill et al. 2018; Hanuš et al. 2018), Jupiter Trojans (Szabó et al. 2017; Ryan et al. 2017), trans-Neptunian objects (Thirouin & Sheppard 2019; Whidden et al. 2019; Thirouin & Sheppard 2022), and interstellar objects (Bolin et al. 2018; Bolin & Lisse 2020). Lightcurve observations of these distant objects use long exposures and read-out modes requiring 10's of seconds resulting in an observation cadence of ~30-60 s.

Only recently, the advent of complementary metal oxide semiconductor (CMOS) cameras (Harding et al. 2016) that can provide continuous imaging at a few Hz or faster have allowed high time resolution observations of asteroids (Purdum et al. 2021; Pomazan et al. 2022). However, the lack of availability of CMOS cameras at most 3 m or larger optical telescope facilities has limited their availability to mostly meter-scale telescopes restricting their use to observing brighter targets ($V < 17$ Beniyama et al. 2022). An alternative method to obtain high-time resolution photometry of asteroids is to measure lightcurve variations along a trailed asteroid detection. If an asteroid moving 10s of "/s is observed with sidereal tracking such that the stars remain stationary in the camera, the asteroid will streak forming an elongated PSF in the direction of its motion (Vereš et al. 2012b).

NEAs moving as fast as a few 10s of "/s can be imaged using non-sidereal tracking at the asteroid's rate of motion resulting in circular PSF asteroid detections while the background stars are trailed (Sharma et al. 2023). If the asteroid is visibly trailed it is possible to measure variations in its brightness along the trail time resolution of the brightness variations is determined by the trail length and the size of the image resolution element provided by the atmospheric seeing or pixel scale. Similar methodology has been used to obtain ~1 ms lightcurve photometry, of stars observed by CCD cameras operated in continuous read mode (Bianco et al. 2009; Daniels et al. 2023), and in serendipitous observations of fast-moving asteroids (Clark et al. 2023). In addition to providing high time-resolution lightcurve photometry of asteroids, streak lightcurves can provide colour estimates if taken in a series of images with several different filters since it provides full lightcurve coverage of rapidly rotating asteroids, minimizing the effect that rotational variations will have on the colour measurements (e.g., Bolin et al. 2020).

In this work we introduce a method that addresses the challenges of determining the colours and rotation periods of rapidly-spinning asteroids by measuring rotation periods and colours from streak asteroid photometry. Our technique gerrymanders the non-sidereal tracking rate to result in the asteroid moving along a CCD column or row at a rate calculated to provide a good signal-to-noise ratio (SNR) and time resolution. Trailed background stars are used to determine the time-resolved photometric calibration. We tested the technique with observations of several 10 m scale NEAs with the MegaCam instrument on the Canada France Hawaii Telescope (Hartman et al. 2006; Gwyn et al. 2012) and extracted the photometry, and determined the rotation periods, and colours of our targets with periodogram analysis.

2 OBSERVATIONS

We observed three NEAs, 2016 GE₁, 2016 CG₁₈, and 2016 EV₈₄, in 2016 (see Table S1 of Bolin et al. (2023a).) with the Queue Ser-

vice Operations (QSO) TOO (QSO program 16AH29, PI R. Jedicke) program using the MegaCam instrument mounted at the prime focus of the 3.6 m CFHT telescope (Hartman et al. 2006). Our targets had r band magnitudes between 17 and 19 and absolute magnitude, H, between 26.7 and 28.5 corresponding to diameters of ~7-15 m assuming an albedo of 0.15 (Harris & Lagerros 2002). The observation of our targets occurred when they were ~0.01 au from the Earth and moving with an angular rate of 0.3 "/s or faster. Seeing was between ~0.6-0.7 " and the CFHT SkyProbe (Cuillandre et al. 2002) showed minimal variations in attenuation during the time of our observations ($\lesssim 0.01$ mag). The observations were taken at airmass ~1.

The TOO CFHT/MegaCam observations were ideal for our program since they needed to occur immediately following the discovery of our targets before they became fainter or went into solar conjunction (Jedicke et al. 2016). MegaCam provided excellent coverage of our targets and the background star field with its ~1 sq. deg. field of view and 0.187" pixel scale. Our 60 s exposures of 2016 CG₁₈, 2016 EV₈₄, and 2016 GE₁ (column 11 of Table S1) were taken in a serial sequence of Sloan Digital Sky Survey (SDSS) g, r and i band filters (Fukugita et al. 1996). Traditional asteroid lightcurve and color observations alternate between filters to minimize the effect of brightness variations due to their rotation (e.g., Bolin et al. 2023d) but MegaCam's 90 s filter exchange time is prohibitive so filter changes were executed only after 2-3 exposures. We note that it is unnecessary to change filters rapidly for rotation periods much less than the exposure time.

If a telescope's non-sidereal tracking rates match the sky-plane velocity of an asteroid it will result in a circular PSF for the target of width θ_c , typically 0.6 to 0.7" in our observations, with a signal-to-noise ratio (SNR) in an exposure of duration t_{exp} of $\text{SNR}_c(t_{\text{exp}})$. We intentionally trailed our target asteroids to measure short term variations in their brightness caused by their rotation. To ensure that the SNR in each 'seeing resolution element' along the trail was sufficient for our photometric purpose the required trail length, θ_t , is given by rearranging Eq. 2 from Shao et al. (2014) et al:

$$\theta_t = \theta_c \left(\frac{\text{SNR}_c(t_{\text{exp}})}{\text{SNR}_t} - 1 \right) \quad (1)$$

where $10 \lesssim \text{SNR}_t \lesssim 20$ is the SNR within an individual resolution element along the trail. The net tracking rate is therefore $\dot{\theta} = \theta_t t_{\text{exp}}^{-1}$ to provide the desired trail length θ_t and the resulting time resolution along the trail, δ_t , is then

$$\delta_t = t_{\text{exp}} \left(\frac{\text{SNR}_c(t_{\text{exp}})}{\text{SNR}_t} - 1 \right)^{-1}. \quad (2)$$

We used 60 s exposures with the expectation that the targets's periods would be on the order of tens of seconds and we would typically take about six images, two in each of three different filters. We tried to target objects with SNR_0 of several 100 resulting in δ_t on the order of seconds.

The MegaCam CCD chips are $383'' \times 862''$ on a side, an aspect ratio of ~2.25, so the telescope's tracking rates were adjusted to result in an asteroid trail in the Y direction to reduce the probability that it would cross a gap between the chips. Overscan, bias, flats, dark and fringe corrections were applied, and zeropoints were obtained from the Elixir pipeline (Magnier & Cuillandre 2004). We used the Canadian Astronomy Data Centre Solar System Object Image Search tool (Gwyn et al. 2012) to predict the chip in which the asteroid's trail would appear (e.g. Fig. 1). A complete description of the extraction and reduction of the time series asteroid trail photometry is available in Section S1 and example lightcurves extracted for observations of

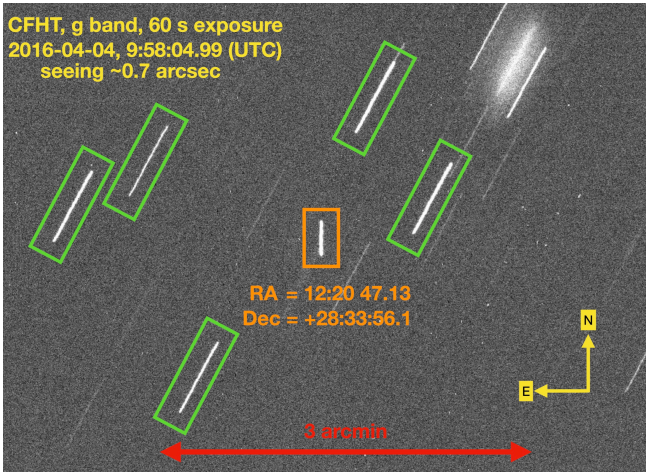


Figure 1. Observation of 2016 GE₁ taken in a 60 s g band exposure with CFHT/MegaCam on 2016-Apr-04. The asteroid is outlined in an orange rectangle. The non-sidereal tracking rate of $\sim 0.32''/s$ was adjusted so the asteroid would only trail in the Y direction. This resulted in the reference background stars trailing in a diagonal direction outlined in green rectangles. The cardinal directions and image scale are indicated on the image.

2016 GE₁, 2016 CG₁₈, and 2016 EV₈₄ are provided in Section S2 of (Bolin et al. 2023a).

We removed secular trends in the lightcurve (e.g., Lindberg et al. 2022) before applying a LS periodogram (LS) periodogram (Lomb 1976; Scargle 1982) to the combined g, r and i lightcurve data to identify periodicity. The top panels of Figs. S5-7 in Bolin et al. (2023a) show the LS periodogram applied to the 2016 GE₁, 2016 CG₁₈, and 2016 EV₈₄ g, r and i lightcurve data. The lightcurve period was determined by using the highest peak above the $3\text{-}\sigma$ false alarm probability level, e.g., the peak in the top panel of Fig. S5 corresponding to a lightcurve period of ~ 15 s. The data were folded using the double-peaked rotation period and rebinned between a phase of 0 and 1 with bin widths of 0.05 and inspected visually (second and third panels of Figs. S5-7). The g-r and r-i colour difference as a function of binned phase are shown in the bottom panel of Figs. S5-7.

3 RESULTS & DISCUSSION

The double-peak rotation period determined from our application of the LS periodogram to the g, r and i data for 2016 GE₁, 2016 CG₁₈, and 2016 EV₈₄ are provided in Table 1. Our dataset had a time resolution of ~ 1 s and the detected rotation periods of our target asteroids are 30-60 s. We applied bootstrap estimation of the uncertainties (Press et al. 1986) by randomly removing \sqrt{N} data points from the time-series lightcurves and repeating the periodogram estimation of the lightcurve period 1,000 times resulting in a $1\text{-}\sigma$ estimate of the lightcurve rotation period uncertainties of 0.01-0.1 s. Our lightcurve observations cover multiple full rotations of the targets (second and third panels of Figs. S5-7 in Bolin et al. 2023a). This is unsurprising given the 750 s to 935 s duration of our lightcurve observations with minimal gaps and the short rotation periods of our targets.

The rotation periods of our three targets are all on the order of tens of seconds, faster than many other observed asteroids in this size range (Fig. 3 and Thirouin et al. (2016); Beniyama et al. (2022)), but considerably longer than the predicted spin periods that are on the order of seconds for 10 m-scale asteroids (Farinella et al. 1998; Vokrouhlický & Čapek 2002; Bolin et al. 2014). The lightcurve

amplitudes are $\sim 0.6\text{-}0.9$ mags (Table 1) providing a rough estimate of the asteroid's b/a axial ratios in the range 1.7-2.3 (Binzel et al. 1989).

Our measured amplitude of ~ 0.8 mag for 2016 GE₁ is significantly larger than the ~ 0.3 mag measured by Warner (2016) on 2016 Apr 5. The difference may be due to the Warner (2016) data having significantly lower SNR (< 10). Differences in the viewing geometry exacerbated by the close approach at ~ 0.01 au, e.g., aspect angle which changed from -26 degrees to 35 degrees in the single day separating the two sets of observations, could also cause extreme changes in the observed lightcurve amplitude (e.g., Barucci & Fulchignoni 1982; Harris et al. 2009). Additionally, photometry submitted around the same time to the Minor Planet Center showed evidence of a significantly larger lightcurve amplitude than 0.3 mag (Warner 2016).

Our measured rotation period for 2016 GE₁ (30.66 ± 0.01 s) is also significantly shorter than the 33.997 ± 0.007 s period ($U = 2$) reported by Warner (2016). The difference in the rotation period between the two dates could be due to 2016 GE₁ being in a tumbling state (e.g., Kaasalainen 2001; Pravec et al. 2005).

The scatter in the g-r and r-i colour measurements for our targets on a bin-by-bin basis is ~ 0.1 magnitudes which may be due to the large error bars for the colour measurements for individual bins. An additional source of scatter could be due to variations in the object's colour with time as seen for 2016 CG₁₈. We estimated the central values of the colours of our targets by taking the weighted average of the binned, phased colour data. The uncertainties are small because the targets were relatively bright, despite being small objects, because they were rapidly targeted in a relatively long exposure with a 4 meter class telescope while near their brightest during their discovery apparition. The r-i colours span the range from bluer to redder than the Sun (Table 1 and Fig. 2). The g-r and r-i colours of 2016 GE₁ and 2016 EV₈₄ overlap the colour-space region generally occupied by S-class asteroids (Ivezić et al. 2001) while 2016 CG₁₈ lies in the border region between the C and S-class. This is as expected since the majority of the small NEA population consists of S-class asteroids (e.g. Jedicke et al. 2018b) and the source probabilities and albedos of the objects are consistent with being S-class inner main belt objects (Table 2 and Nesvorný et al. 2023; Morbidelli et al. 2020).

The g-r, r-i colours and spectral slope of 2016 GE₁ (g-r = 0.66 ± 0.01 , r-i = 0.20 ± 0.01 , g-i = 0.86 ± 0.01 , spectral gradient = $9.2 \pm 0.3\%$) are broadly consistent with being classified as an S-type (S-type spectral gradient = 6-25% DeMeo & Carry 2013).

The g-r and r-i colours and spectral of 2016 CG₁₈ (g-r = 0.58 ± 0.01 , r-i = 0.17 ± 0.01 , g-i = 0.75 ± 0.04 , spectral gradient = $6.9 \pm 0.3\%$) and 2016 EV₈₄ (g-r = 0.70 ± 0.02 , r-i = 0.05 ± 0.04 , g-i = 0.75 ± 0.04 , spectral gradient = $6.9 \pm 1.3\%$) are consistent with being classified as an X-class asteroid (X-class spectral gradient = 3-9%, DeMeo & Carry 2013). Asteroids belonging to both the X and S-type classes are found in the inner-Main belt (DeMeo & Carry 2013). Devogèle et al. (2019) found that 2016 CG₁₈ has a Xe-type spectrum using visible spectroscopy aligning with our results that it has X-complex colours.

4 CONCLUSIONS

We have demonstrated the use of an asteroid streak lightcurve technique on three ~ 10 m-scale asteroids, 2016 GE₁, 2016 CG₁₈, and 2016 EV₈₄, and compared the results with existing data. The asteroid streak technique may be applicable in the future when using CCD cameras to study fast-rotating asteroids. In addition, the increased

Table 1. Rotation periods and colours.

object name	period (s)	amplitude (mag)	b/a ratio	m_r (mag)	g-r (mag)	r-i (mag)
2016 CG ₁₈	55.180±0.036	0.62±0.07	1.77±0.11	17.29±0.01	0.58±0.01	0.17±0.01
2016 EV ₈₄	52.237±0.062	0.86±0.16	2.21±0.32	18.89±0.01	0.70±0.02	0.05±0.04
2016 GE ₁	30.664±0.007	0.78±0.05	2.05±0.10	17.34±0.01	0.66±0.01	0.20±0.01
Solar colours					0.46±0.01	0.12±0.01

Notes. (1) double-peak rotation period, (2) r-band peak-to-peak lightcurve amplitude, (3) Apparent r-band magnitude, (4) solar colours from Haberreiter et al. (2017) and Willmer (2018).

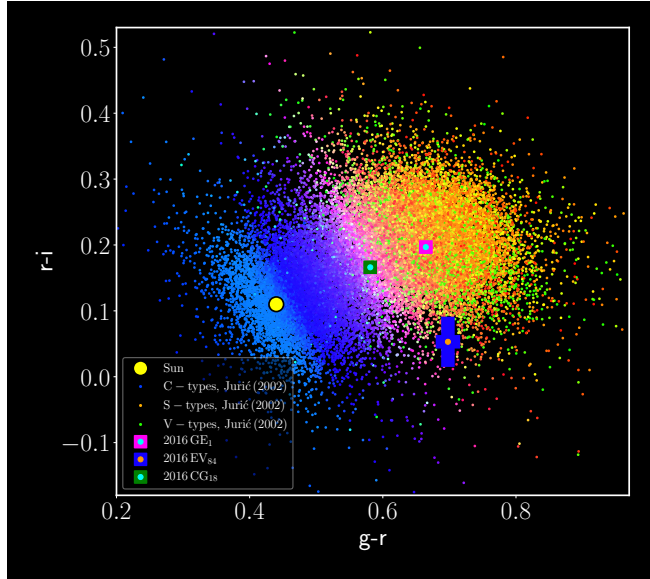


Figure 2. g-r vs r-i colours for 2016 GE₁, 2016 CG₁₈, and 2016 EV₈₄ superimposed on main belt asteroid colours from the SDSS (Ivezić et al. 2001; Jurić et al. 2002). The circular yellow marker indicates the Sun’s colours (See Table 1.)

Table 2. Main belt source region probabilities and albedos.

object	ν_6	3:1	Inner	Hungaria	albedo
2016 CG ₁₈	0.75	0.14	0.02	0.09	0.21
2016 EV ₈₄	0.72	0.17	0.05	0.06	0.20
2016 GE ₁	0.75	0.12	0.11	0.02	0.19

Notes. Main belt source probabilities according to the NEO model of Nesvorný et al. (2023) for sources that have > 1% probability for these objects. i.e. the ν_6 and 3:1 resonances, the ‘Inner’ main belt source, and the Hungaria family. Albedos of the objects as predicted by Morbidelli et al. (2020).

lightcurve coverage may improve the measurement of the physical properties of asteroids using optical CCDs that are too difficult to observe by other means due to having a short timespan of observability, e.g. in the case of close-approaching asteroids (Jedicke et al. 2018a; Farnocchia et al. 2022), or proximity to the Sun, e.g. interior-Earth objects (e.g., Bolin et al. 2022, 2023b).

ACKNOWLEDGEMENTS

Based on observations obtained with MegaPrime/MegaCam, a joint project of CFHT and CEA/DAPNIA, at the Canada-France-Hawaii Telescope (CFHT) which is operated by the National Research Council (NRC) of Canada, the Institut National des Science de l’Univers of the Centre National de la Recherche Scientifique (CNRS) of France,

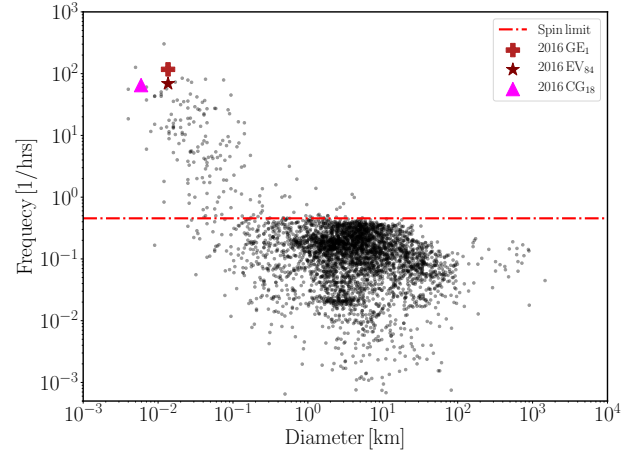


Figure 3. Rotation frequency vs. diameter for asteroids in the Asteroid Lightcurve Database with quality codes U=2,3 (Warner et al. 2009) and the rotation periods for 2016 GE₁, 2016 CG₁₈, and 2016 EV₈₄ from this work. The diameters, D of our 3 targets were calculated from their absolute magnitude and an assumed albedo, $p \approx 0.25$, typical of small S-type asteroids (Morbidelli et al. 2020; Bolin et al. 2023c), with $D = 1329 p^{-1/2} 10^{-H/5}$ (Russell 1916). The spin barrier frequency corresponding to a period of ~ 2.2 h is indicated with a horizontal red dash-dotted line (Polishook et al. 2016).

and the University of Hawaii. The observations at the Canada-France-Hawaii Telescope were performed with care and respect from the summit of Maunakea which is a significant cultural and historic site. B.T.B. is supported by an appointment to the NASA Postdoctoral Program at the NASA Goddard Space Flight Center, administered by Oak Ridge Associated Universities under contract with NASA. M.G. was supported by the Research Experiences for Undergraduates program at the Institute for Astronomy, Univ. of Hawai‘i at Mānoa.

DATA AVAILABILITY

The data underlying this article will be shared on reasonable request to the corresponding author.

SUPPLEMENTAL MATERIAL

The supplemental material for this manuscript is available online.

REFERENCES

- Barucci M. A., Fulchignoni M., 1982, *Moon and Planets*, **27**, 47
Beniyama J., et al., 2022, *PASJ*, **74**, 877

- Bianco F. B., Protopapas P., McLeod B. A., Alcock C. R., Holman M. J., Lehner M. J., 2009, *AJ*, **138**, 568
- Binzel R. P., Farinella P., Zappalà V., Cellino A., 1989, in Binzel R. P., Gehrels T., Matthews M. S., eds, *Asteroids II*. pp 416–441
- Bolin B. T., Lisse C. M., 2020, *MNRAS*, **497**, 4031
- Bolin B., et al., 2014, *Icarus*, **241**, 280
- Bolin B. T., et al., 2018, *ApJ*, **852**, L2
- Bolin B. T., et al., 2020, *ApJ*, **900**, L45
- Bolin B. T., et al., 2022, *MNRAS*, **517**, L49
- Bolin B. T., Ghosal M., Jedicke R., 2023a, Supplemental Material.
- Bolin B. T., Ahumada T., Dokkum P. v., Fremling C., Hardegree-Ullman K. K., Purdum J. N., Serabyn E., Southworth J., 2023b, *Icarus*, **394**, 115442
- Bolin B. T., Noll K. S., Caiazzo I., Fremling C., Binzel R. P., 2023c, *Icarus*, **400**, 115562
- Bolin B. T., et al., 2023d, *MNRAS*, **521**, L29
- Bottke W. F., Durda D. D., Nesvorný D., Jedicke R., Morbidelli A., Vokrouhlický D., Levison H., 2005a, *Icarus*, **175**, 111
- Bottke W. F., Durda D. D., Nesvorný D., Jedicke R., Morbidelli A., Vokrouhlický D., Levison H. F., 2005b, *Icarus*, **179**, 63
- Bottke Jr. W. F., Vokrouhlický D., Rubincam D. P., Nesvorný D., 2006, *Annual Review of Earth and Planetary Sciences*, **34**, 157
- Clark D. L., Wiegert P. A., Brown P. G., Vida D., Heinze A., Denneau L., 2023, *Planetary Science Journal*, **4**, 103
- Cuillandre J.-C., Magnier E. A., Isani S., Sabin D., Knight W., Kras S., Lai K., 2002, in Quinn P. J., ed., *Society of Photo-Optical Instrumentation Engineers (SPIE) Conference Series Vol. 4844, Observatory Operations to Optimize Scientific Return III*. pp 501–507, doi:10.1117/12.460613
- Daniels S., Bianco F. B., Andreoni I., Mahabal A., 2023, in prep.
- DeMeo F. E., Carry B., 2013, *Icarus*, **226**, 723
- Devogèle M., et al., 2019, *AJ*, **158**, 196
- Farinella P., Vokrouhlický D., Hartmann W. K., 1998, *Icarus*, **132**, 378
- Farnocchia D., et al., 2022, *Planetary Science Journal*, **3**, 156
- Fraser W. C., Pravec P., Fitzsimmons A., Lacerda P., Bannister M. T., Snodgrass C., Smolić I., 2018, *Nature Astronomy*, **2**, 383
- Fukugita M., Ichikawa T., Gunn J. E., Doi M., Shimasaku K., Schneider D. P., 1996, *AJ*, **111**, 1748
- Gwyn S. D. J., Hill N., Kavelaars J. J., 2012, *PASP*, **124**, 579
- Haberreiter M., Schöll M., Dudok de Wit T., Kretzschmar M., Misios S., Tourpali K., Schmutz W., 2017, *Journal of Geophysical Research (Space Physics)*, **122**, 5910
- Hanuš J., et al., 2018, *Icarus*, **299**, 84
- Harding L. K., et al., 2016, *MNRAS*, **457**, 3036
- Harris A. W., Lagerros J. S. V., 2002, *Asteroids III*, pp 205–218
- Harris A. W., Fahnestock E. G., Pravec P., 2009, *Icarus*, **199**, 310
- Hartman J. D., Bersier D., Stanek K. Z., Beaulieu J. P., Kaluzny J., Marquette J. B., Stetson P. B., Schwarzenberg-Czerny A., 2006, *MNRAS*, **371**, 1405
- Hirabayashi M., 2015, *MNRAS*, **454**, 2249
- Ivezić Ž., et al., 2001, *AJ*, **122**, 2749
- Jedicke R., Granvik M., Micheli M., Ryan E., Spahr T., Yeomans D. K., 2015, *Asteroids IV*, pp 795–813
- Jedicke R., Bolin B., Granvik M., Beshore E., 2016, *Icarus*, **266**, 173
- Jedicke R., Bolin B. T., Bottke W. F., Chyba M., Fedorets G., Granvik M., Jones L., Urrutxua H., 2018a, *Frontiers in Astronomy and Space Sciences*, **5**, 13
- Jedicke R., Sercel J., Gillis-Davis J., Morenz K. J., Gertsch L., 2018b, *Planet. Space Sci.*, **159**, 28
- Jenniskens P., et al., 2010, *Meteoritics and Planetary Science*, **45**, 1590
- Jurić M., et al., 2002, *AJ*, **124**, 1776
- Kaasalainen M., 2001, *A&A*, **376**, 302
- Kozubal M. J., Gasdía F. W., Dantowitz R. F., Scheirich P., Harris A. W., 2011, *Meteoritics & Planetary Science*, **46**, 534
- Lindberg C. W., et al., 2022, *AJ*, **163**, 29
- Lomb N. R., 1976, *Ap&SS*, **39**, 447
- Magnier E. A., Cuillandre J. C., 2004, *PASP*, **116**, 449
- McNeill A., et al., 2018, *AJ*, **156**, 282
- Micheli M., Tholen D. J., Elliott G. T., 2013, *Icarus*, **226**, 251
- Micheli M., Tholen D. J., Elliott G. T., 2014, *ApJ*, **788**, L1
- Morbidelli A., Delbo M., Granvik M., Bottke W. F., Jedicke R., Bolin B., Michel P., Vokrouhlický D., 2020, *Icarus*, **340**, 113631
- Nesvorný D., et al., 2023, *AJ*, **166**, 55
- Polishook D., et al., 2016, *Icarus*, **267**, 243
- Pomazan A., Tang Z.-H., Maigurova N., Yu Y., Tang K., Mao Y.-D., Song Y.-Z., 2022, *Planet. Space Sci.*, **216**, 105477
- Pravec P., et al., 2005, *Icarus*, **173**, 108
- Press W. H., Flannery B. P., Teukolsky S. A., 1986, *Numerical recipes. The art of scientific computing*
- Purdum J. N., et al., 2021, *ApJ*, **911**, L35
- Russell H. N., 1916, *ApJ*, **43**, 173
- Ryan E. L., Sharkey B. N. L., Woodward C. E., 2017, *AJ*, **153**, 116
- Sánchez P., Scheeres D. J., 2014, *Meteoritics and Planetary Science*, **49**, 788
- Scargle J. D., 1982, *ApJ*, **263**, 835
- Shao M., Nemati B., Zhai C., Turyshev S. G., Sandhu J., Hallinan G., Harding L. K., 2014, *ApJ*, **782**, 1
- Sharma K., et al., 2023, *MNRAS*, **524**, 2651
- Szabó R., et al., 2016, *A&A*, **596**, A40
- Szabó G. M., et al., 2017, *A&A*, **599**, A44
- Thirouin A., Sheppard S. S., 2019, *AJ*, **157**, 228
- Thirouin A., Sheppard S. S., 2022, *Planetary Science Journal*, **3**, 178
- Thirouin A., et al., 2016, *AJ*, **152**, 163
- Vereš P., Jedicke R., Denneau L., Wainscoat R., Holman M. J., Lin H., 2012a, *PASP*
- Vereš P., Jedicke R., Denneau L., Wainscoat R., Holman M. J., Lin H.-W., 2012b, *PASP*, **124**, 1197
- Virtanen P., et al., 2020, *Nature Methods*, **17**, 261
- Vokrouhlický D., Čapek D., 2002, *Icarus*, **159**, 449
- Vokrouhlický D., Bottke W. F., Chesley S. R., Scheeres D. J., Statler T. S., 2015, *Asteroids IV*, pp 509–531
- Warner B. D., 2016, *Minor Planet Bulletin*, **43**, 240
- Warner B. D., Harris A. W., Pravec P., 2009, *Icarus*, **202**, 134
- Whidden P. J., et al., 2019, *AJ*, **157**, 119
- Willmer C. N. A., 2018, *ApJS*, **236**, 47

SUPPLEMENTAL MATERIAL

In this Supplemental Material section, we provide a detailed mathematical description of the methodology of our technique for extracting and calibrating asteroid streak photometry (Section S1), the application of the method to real asteroid streak data (Section S2), and the determination of asteroid rotation period and colours (Section S3). The methodological description is presented as a general guideline leaving the exact implementation of the streak extraction method to the needs of the user. The asteroid lightcurves in Section S1 are presented to illustrate the periodic variations in their brightness. The periodogram and colour analysis described in Section S3 details the application of our method and results for each of our asteroid targets.

S1 Asteroid trail extraction and calibration

Each image was visually inspected to identify the asteroid trail and measure the approximate coordinates of its centroid. We then fit the asteroid source to a Gaussian point spread function convolved with a straight line following Vereš et al. (2012a):

$$f(x, y) = B + \frac{\Phi}{2\sigma L\sqrt{2\pi}} \exp\left(-\frac{((x-x_0)\sin\phi_0 + (y-y_0)\cos\phi_0)^2}{2\sigma^2}\right) \left[\operatorname{erf}\left(\frac{(x-x_0)\cos\phi_0 + (y-y_0)\sin\phi_0 + L/2}{\sigma\sqrt{2}}\right) - \operatorname{erf}\left(\frac{(x-x_0)\cos\phi_0 + (y-y_0)\sin\phi_0 - L/2}{\sigma\sqrt{2}}\right) \right] \quad (\text{S1})$$

where (x_0, y_0) represent the pixel coordinates of the trail's centroid, ϕ_0 is the angle made by the trail relative to the positive x -axis, L is the trail length, σ is the standard deviation of the Gaussian representing the point spread function (PSF), Φ is the total flux in the trail, and B represents the background sky. The fit was obtained with `Scipy.optimize.curve_fit` which also provides the $1\text{-}\sigma$ uncertainties on the fitted parameters.

As an example, the center of 2016 GE₁'s trail varies from row to row as a consequence of the imperfect tracking of the telescope and time-varying and localized seeing (top panel of Fig. S1) but `curve_fit` returns the row-averaged centroid (middle panel of Fig. S1). The fitted trail defines the trail start and ending points and the trail width necessary for reducing the light curve.

Prior to extracting lightcurves from the asteroid trails, each frame was rotated by $-\phi_0$ degrees using the flux-conserving routine provided by `Scipy.ndimage.rotate` (Virtanen et al. 2020) resulting in asteroid trails exactly aligned with the CCD columns. ϕ_0 was not 0° or 90° because the orbits of the NEOs at the time of observation were not well constrained so our calculation of the non-sidereal tracking rates could introduce a small tracking error resulting in a misaligned trail.

Once the trails were oriented along CCD columns the row number is linearly correlated with time. The physical rotation of the asteroid will result in a time-varying flux along the rows if the asteroid is rotating and not spherical or has surface albedo variations. Non-sidereal tracking errors could also appear as a small time-varying flux, though inspection of nearby star trails shows this to be smaller than a few percent.

While the fitted trail parameters are real numbers, our light curve reduction is integer pixel-based. We define the integer number of pixels in one full-width-at-half-maximum (FWHM) of the PSF as

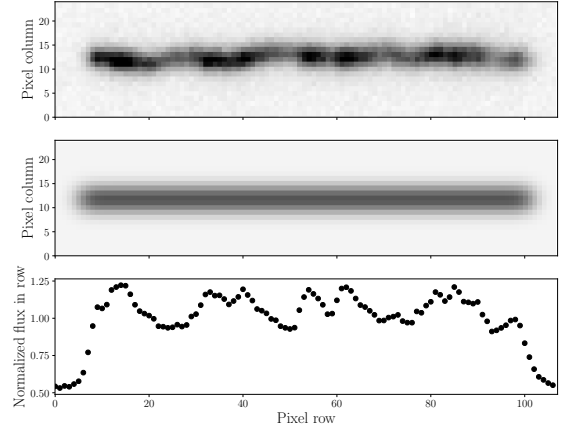


Figure S1. Top panel: asteroid 2016 GE₁ trail from 4 April 2016 rotated by 90° . Middle panel: the same trail as realized from the Vereš et al. (2012a) trail fit Eq. S1. The wiggling appearance of the trail in the perpendicular direction is due to the imperfect tracking of the telescope. Bottom panel: the sum of the flux in each column versus column number normalized by the median of the lightcurve. The flux has not yet been corrected for sky background and transparency. The ends of the lightcurve fall to ~ 0.5 because they sample the background sky.

$n_w = \text{ceil}(2.355 \sigma)$. The fitted trail's endpoints are given by

$$(x_1, y_1) = (x_0, y_0 + L/2) \quad (\text{S2})$$

$$(x_2, y_2) = (x_0, y_0 - L/2) \quad (\text{S3})$$

but we truncate the trail on each end by n_w pixels to eliminate edge effects at the beginning and end of the exposure. Thus, the effective trail length is $L = L_0 - 2n_w$ pixels.

Letting $i_n = \text{int}(x_n)$ represent the column/pixel number containing the position x_n and $j_n = \text{int}(y_n)$ represent the row number containing the position y_n , the integer pixel bounds for the asteroid's signal are:

$$\begin{aligned} i_{min} &= \text{floor}(x_0 - n_w) \\ i_{max} &= \text{ceil}(x_0 + n_w) \\ j_{min} &= \text{floor}(y_0 - L/2) \\ j_{max} &= \text{ceil}(y_0 + L/2) \end{aligned} \quad (\text{S4})$$

The total flux in each row m through n inclusive is:

$$F_j = \sum_{j=m}^n \sum_{i=i_{min}}^{i_{max}} F_{ij} \quad (\text{S5})$$

where F_{ij} is the flux in pixel (i, j) .

The contribution of the sky background to the asteroid flux is calculated using a set of pixels adjacent to the streak. The bounds in i are identical to those in Eq. S4 but the bounds in j are:

$$\begin{aligned} i_{-min} &= i_0 - n_w \\ i_{-max} &= i_0 - n_{sky} \\ i_{+min} &= i_0 + n_w \\ i_{+max} &= i_0 + n_{sky} \end{aligned} \quad (\text{S6})$$

where $n_{sky} = 4 n_w$ and the $-$ and $+$ subscripts denote the sky region left and right of the trail, respectively. The total number of sky pixels is then $N_{sky} = 2(n_{sky} - n_w)$ and the total flux in the sky background

region in row j bracketing the asteroid trail is:

$$F_{sky,j} = \sum_{i=i_{-min}}^{i_{-max}} F_{ij} + \sum_{i=i_{+min}}^{i_{+max}} F_{ij}. \quad (S7)$$

The average background flux per pixel in the region surrounding, and presumably beneath, the trail is then $\bar{F}_{sky,j} = F_{sky,j}/N_{sky}$. Finally, the background-corrected signal in the j^{th} row of the trail is:

$$S_j = F_j - N_{sky} \bar{F}_{sky,j} \quad (S8)$$

The error on the background-subtracted flux as a function of row number is

$$\sigma_j^2 = \frac{F_j}{G} + n_w \left(\frac{\bar{F}_{sky,j}}{G} + R^2 \right) + n_w^2 \sigma_{sky,j}^2 \quad (S9)$$

where G is the CCD gain, the number of CCD ‘counts’ per e^- , R is the read noise of the electronics in e^-/pixel , and $\sigma_{sky,j} = \sqrt{\bar{F}_{sky,j}}/N_{sky}$. The calibrated magnitude in the j^{th} row of the trail is:

$$M_j = -2.5 * \log_{10}(S_j) + ZP \quad (S10)$$

where ZP is the zerpoint obtained from Elixir photometry.

S2 Asteroid streak lightcurves

The asteroid streak lightcurve extraction procedure described in Section S1 was applied to the g, r, and i images taken for 2016 GE₁, 2016 CG₁₈, and 2016 EV₈₄ (observational circumstances described in Table S1).

The combined g, r and i lightcurves for 2016 GE₁ (top panel of Fig. S2) show clear evidence of the asteroid’s colours (discussed below) while the individual g, r and i lightcurves (panels 2-4 of Fig. S2) show the sinusoidal shape typical for a prolate spinning body (Barucci & Fulchignoni 1982). The amplitude in the g and r lightcurve data is ~ 0.8 magnitudes though it is reduced in the i band, possibly due to tumbling of the asteroid (e.g., Fraser et al. 2018).

The combined g, r and i lightcurves for 2016 CG₁₈ (top panel of Fig. S3) show clear evidence of the asteroid’s colours (discussed below) while the individual g, r and i lightcurves (panels 2-4 of Fig. S3) show an indication of a sinusoidal lightcurve shape that is more prominent in the r band images compared to the g and i band images. The r band lightcurve has an amplitude of ~ 0.6 magnitudes, but is diminished compared to the scatter in the g and i band lightcurves which could be due to tumbling motion or the lower SNR of the g and i band data.

The combined g, r and i lightcurves for 2016 EV₈₄ (top panel of Fig. S4) again shows evidence of the asteroid’s colours (discussed below) while the individual g and r lightcurves (panels 2-3 of Fig. S4) show a sinusoidal shape with an amplitude of ~ 0.9 mags. The i band lightcurve (panels 4 of Fig. S4) shows a hint of a sinusoidal shape but an amplitude comparable to the scatter in the lightcurve.

S3 Periods and colours

We applied the Lomb-Scargle periodogram (LS) (Lomb 1976; Scargle 1982) to the combined, detrended g, r and i lightcurve data to determine the rotation period of our three asteroids (top panels of Figs. S5-7). The maximum period in the LS periodogram search was the total time span of the observations (column 13 in Table S1). For 2016 CG₁₈, the maximum period in the LS periodogram search was the total duration of the r band images (~ 140 s) which is much more

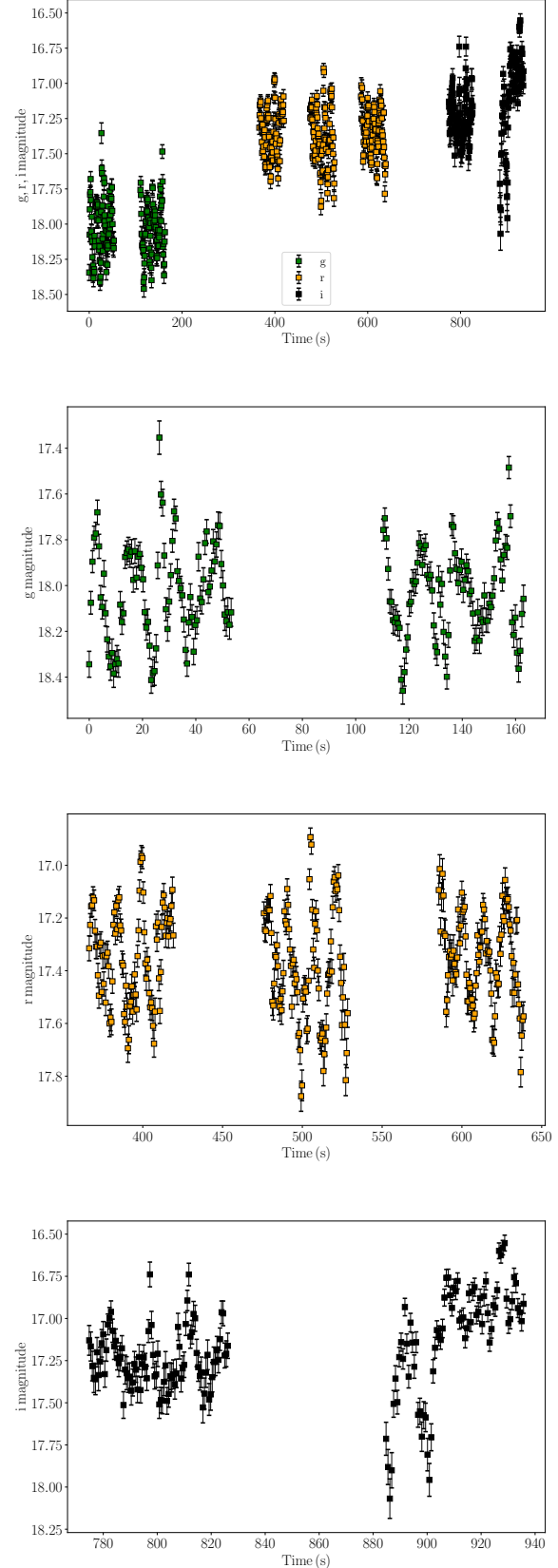


Figure S2. Lightcurves in g, r and i bands from CFHT/MegaCam observations of 2016 GE₁ taken 2016 Apr 04. The total duration of the observations is ~ 960 s. First panel: combination all 3 bands. Second panel: g-band. Third panel: r-band. Fourth panel: i-band.

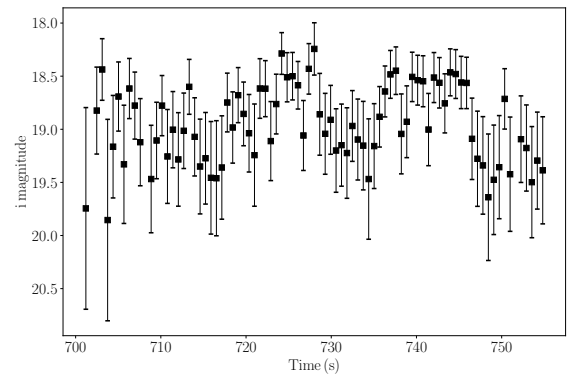
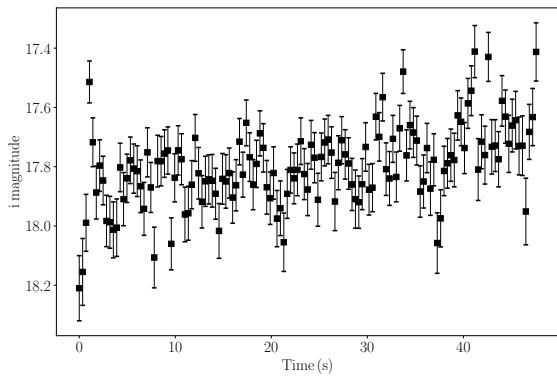
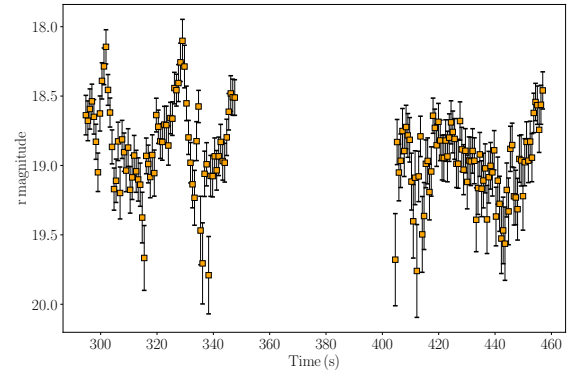
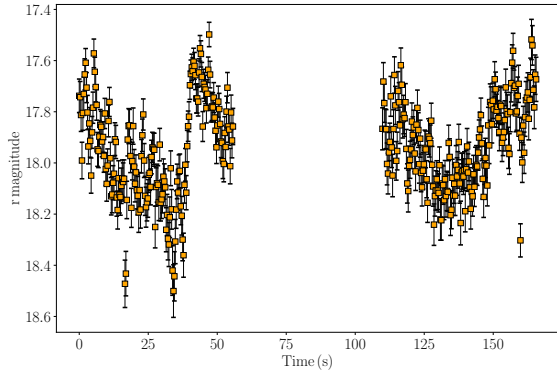
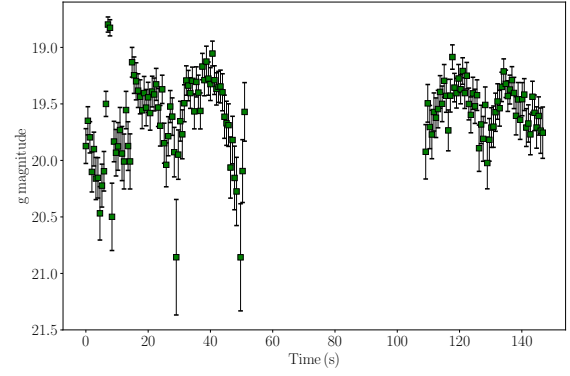
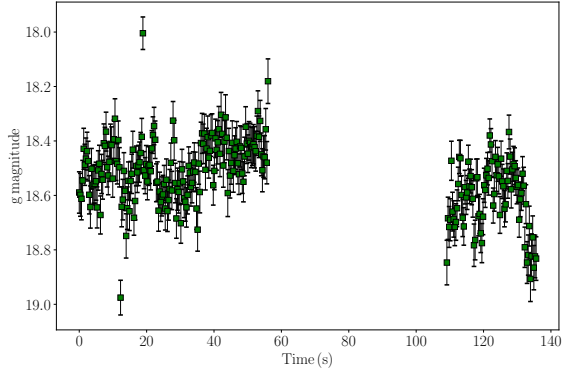
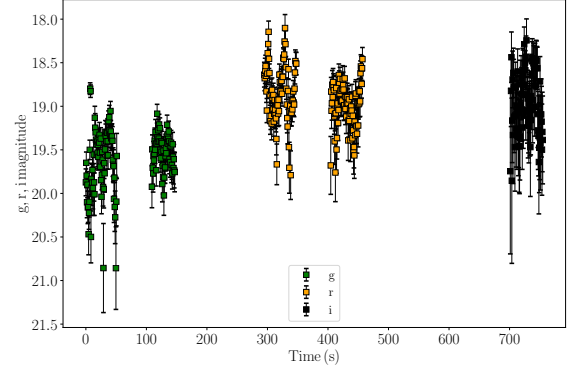
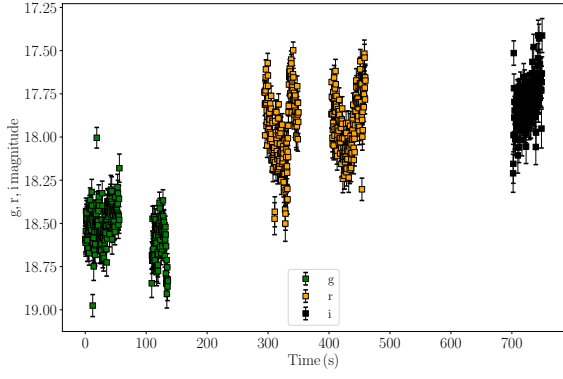


Figure S3. Lightcurves in g, r and i bands from CFHT/MegaCam observations of 2016 CG₁₈ taken 2016 Feb 05. The total duration of the observations is ~ 750 s. First panel: combination all 3 bands. Second panel: g-band. Third panel: r-band. Fourth panel: i-band.

Figure S4. Lightcurves in g, r and i bands from CFHT/MegaCam observations of 2016 EV₈₄ taken 2016 Mar 12. The total duration of the observations is ~ 755 s. First panel: combination all 3 bands. Second panel: g-band. Third panel: r-band. Fourth panel: i-band.

than the found lightcurve period (~ 28 s, top panel of Fig. S6). We applied bootstrap estimation of the uncertainties (Press et al. 1986) by randomly removing \sqrt{N} data points from the time-series lightcurves and repeating the periodogram estimation of the lightcurve period 1,000 times resulting in a $1-\sigma$ estimate of the lightcurve rotation period uncertainties of 0.01-0.1 s. The g, r and i lightcurves were then folded assuming a double-peak rotational lightcurve (second panels of Figs. S5-7) and re-binned with bin widths of 0.05 for phases in the range 0-1 (third panel of Figs. S5-7). Finally, the g-r and r-i colour differences were calculated as a function of phase (bottom panels of Figs. S5-7).

2016 GE₁'s LS power spectrum peak indicates a lightcurve period of ~ 15 s (top panel of Fig. S5) implying a double-peak rotation period of ~ 31 s that was used for folding the lightcurve data (second and third panel of Fig. S5). The weighted mean g-r colour for 2016 EV₈₄ is $\sim 0.66 \pm 0.01$ and the weighted mean r-i colours is $\sim 0.20 \pm 0.01$ (fourth panel of Fig. S5).

2016 CG₁₈'s LS power spectrum peak indicates a lightcurve period of ~ 28 s (top panel of Fig. S6) implying a double-peak rotation period of ~ 56 s that was used for folding the lightcurve data (second and third panel of Fig. S6). The weighted mean g-r colour for 2016 EV₈₄ is $\sim 0.58 \pm 0.01$ and the weighted mean r-i colours is $\sim 0.17 \pm 0.01$ (fourth panel of Fig. S6).

2016 EV₈₄'s LS power spectrum peak indicates a lightcurve period of ~ 26 s (top panel of Fig. S7) implying a double-peak rotation period of ~ 52 s that was used for folding the lightcurve data (second and third panel of Fig. S7). The weighted mean g-r colour for 2016 EV₈₄ is $\sim 0.70 \pm 0.02$ and the weighted mean r-i colours is $\sim 0.05 \pm 0.04$ (fourth panel of Fig. S7).

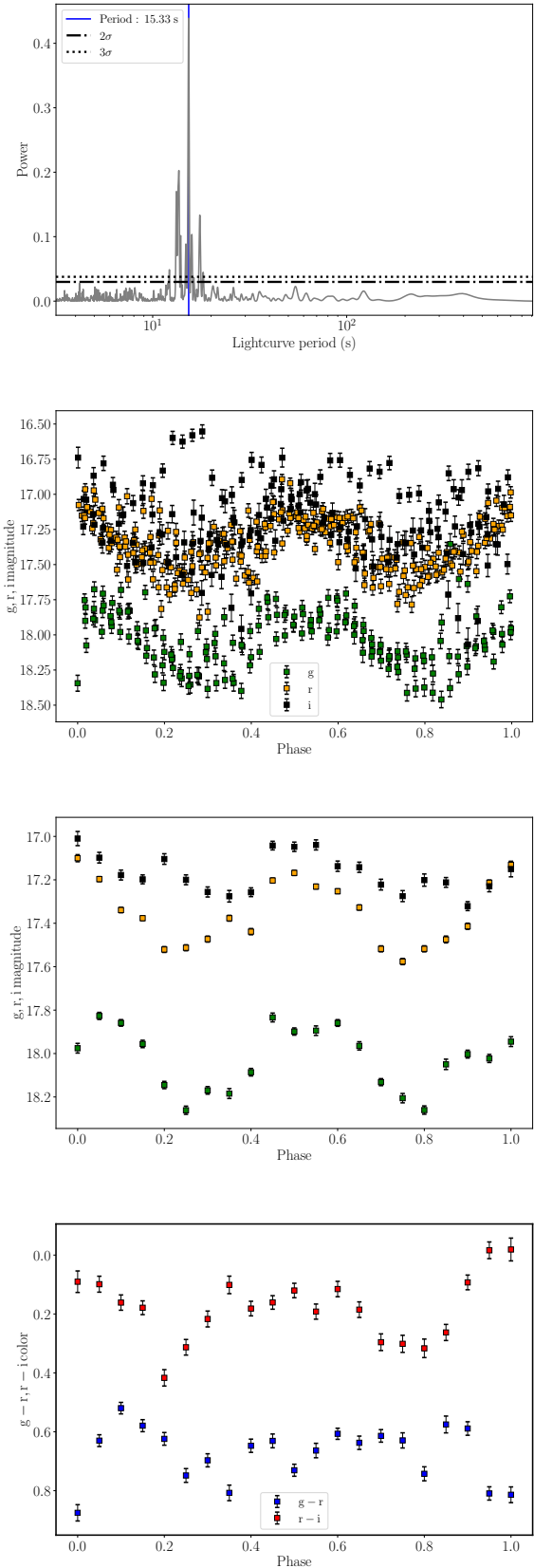


Figure S5. Top panel: Lomb-Scargle periodogram of the r-band data for 2016 GE₁. The $2-\sigma$ and $3-\sigma$ false alarm probabilities are shown as dotted and dashed-dotted lines respectively. A local maxima of ~ 15.3 s is indicated with a vertical blue line. Second panel: the g, r and i-band lightcurve data of 2016 GE₁ folded with a rotation period of ~ 31 s. Third panel: The g, r and i lightcurve data of 2016 GE₁ folded to a rotation period of ~ 31 s and rebinned with a phase bin size of 0.05. Fourth panel: g-r and r-i rebinned and folded colour curves of 2016 GE₁.

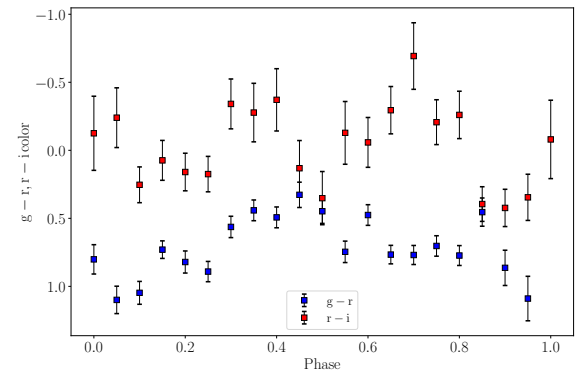
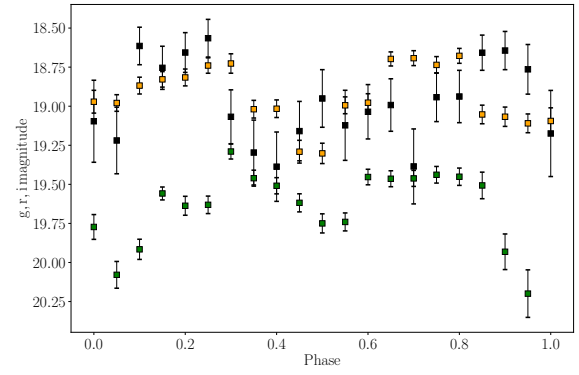
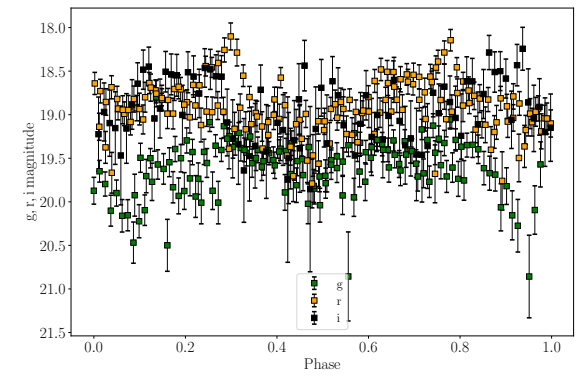
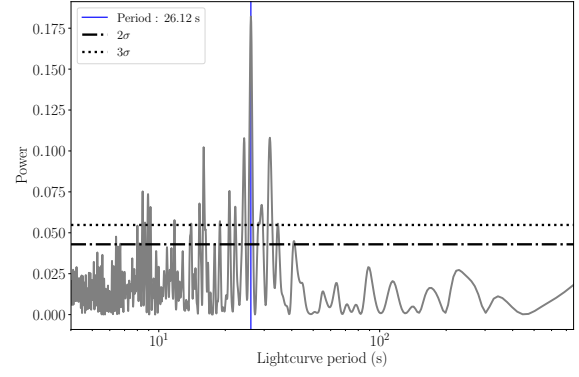
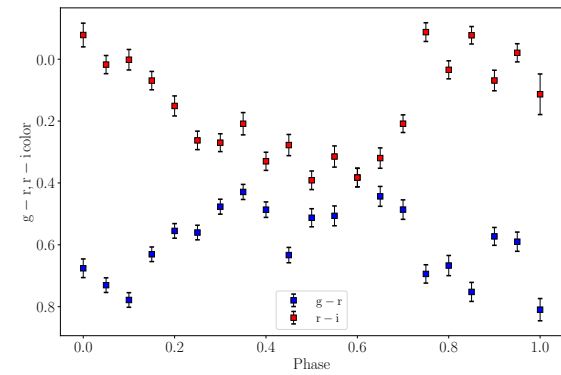
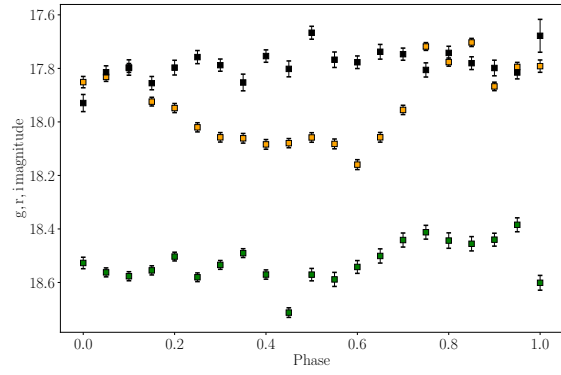
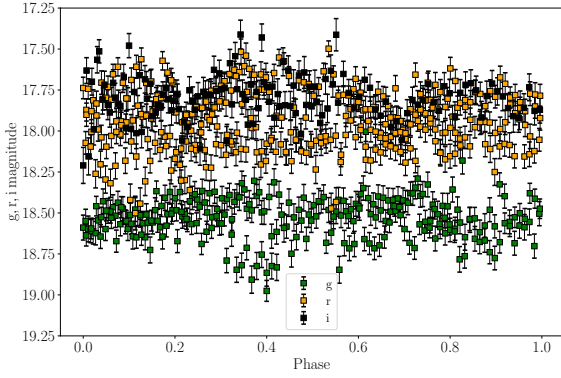
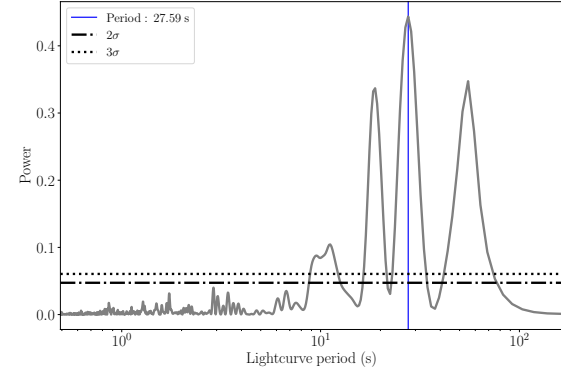


Figure S6. Top panel: Lomb-Scargle periodogram of the r-band data for 2016 CG₁₈. The 2- σ and 3- σ false alarm probabilities are shown as dotted and dashed-dotted lines respectively. A local maxima of ~ 28 s is indicated with a vertical blue line. Second panel: the g, r and i-band lightcurve data of 2016 CG₁₈ folded with a rotation period of ~ 56 s. Third panel: The g, r and i lightcurve data of 2016 CG₁₈ folded to a rotation period of ~ 56 s and rebinned with a phase bin size of 0.05. Fourth panel: g-r and r-i rebinned and folded colour curves of 2016 CG₁₈.

Figure S7. Top panel: Lomb-Scargle periodogram of the r-band data for 2016 EV₈₄. The 2- σ and 3- σ false alarm probabilities are shown as dotted and dashed-dotted lines respectively. A local maxima of ~ 26 s is indicated with a vertical blue line. Second panel: the g, r and i-band lightcurve data of 2016 EV₈₄ folded with a rotation period of ~ 52 s. Third panel: The g, r and i lightcurve data of 2016 EV₈₄ folded to a rotation period of ~ 52 s and rebinned with a phase bin size of 0.05. Fourth panel: g-r and r-i rebinned and folded colour curves of 2016 EV₈₄.

Table S1. Observational details.

object name	a ⁽¹⁾ (au)	e ⁽²⁾	i ⁽³⁾ (deg)	H ⁽⁴⁾ (mag)	Date UTC	R_H ⁽⁵⁾ (au)	Δ ⁽⁶⁾ (au)	α ⁽⁷⁾ ($^\circ$)	θ_s ⁽⁸⁾ ($''$)	χ_{am} ⁽⁹⁾	g,r,i obs ⁽¹⁰⁾	ΔT ⁽¹¹⁾ (s)	$\delta\dot{\theta}$ ⁽¹²⁾ ($''/s$)	θ_t ⁽¹³⁾ ($''$)	N_{θ_t} ⁽¹⁴⁾	δt ⁽¹⁵⁾ (s)	m_r ⁽¹⁶⁾ (mag)
2016 CG ₁₈	1.06	0.12	5.31	28.5	2016 Feb 05-13:52	0.989	0.004	45.4	0.56	1.14	2,2,2	749.6	0.55	33.1	59.1	1.01	17.29±0.01
2016 EV ₈₄	0.87	0.18	13.62	26.7	2016 Mar 12-09:17	1.011	0.018	14.4	0.71	1.03	2,2,1	754.8	0.28	16.8	23.7	2.53	18.89±0.01
2016 GE ₁	2.10	0.53	10.77	26.7	2016 Apr 04-10:07	1.007	0.009	41.8	0.67	1.01	2,3,2	935.8	0.32	19.3	28.8	2.08	17.34±0.01

Notes. (1) semi-major axis, (2) eccentricity, (3) inclination, (4) absolute magnitude, (5) heliocentric distance, (6) geocentric distance, (7) phase angle, (8) seeing FWHM measured using image background stars, (9) airmass measured at chip-center, (10) number of g, r and i exposures, (11) duration of entire g, r and i sequence, (12) net difference between target movement rate and the tracking rate of the telescope, (13) asteroid trail length, (14) number of resolution elements in asteroid trail, (15) time resolution element per unit of spatial resolution along asteroid trail, (16) apparent r-band magnitude.

This paper has been typeset from a $\text{\TeX}/\text{\LaTeX}$ file prepared by the author.